# A Hybrid Finite-Difference-Particle Method for Chemotaxis Models

Alina Chertock*, Shumo Cui†, Alexander Kurganov‡, and Chenxi Wang§

**Abstract**

Chemotaxis systems play a crucial role in modeling the dynamics of bacterial and cellular behaviors, including propagation, aggregation, and pattern formation, all under the influence of chemical signals. One notable characteristic of these systems is their ability to simulate concentration phenomena, where cell density undergoes rapid growth near specific concentration points or along certain curves. Such growth can result in singular, spiky structures and lead to finite-time blowups.

Our investigation focuses on the dynamics of the Patlak-Keller-Segel chemotaxis system and its two-species extensions. In the latter case, different species may exhibit distinct chemotactic sensitivities, giving rise to very different rates of cell density growth. Such a situation may be extremely challenging for numerical methods as they may fail to accurately capture the blowup of the slower-growing species mainly due to excessive numerical dissipation.

In this paper, we propose a hybrid finite-difference-particle (FDP) method, in which a particle method is used to solve the chemotaxis equation(s), while finite difference schemes are employed to solve the chemoattractant equation. Thanks to the low-dissipation nature of the particle method, the proposed hybrid scheme is particularly adept at capturing the blowup behaviors in both one- and two-species cases. The proposed hybrid FDP methods are tested on a series of challenging examples, and the obtained numerical results demonstrate that our hybrid method can provide sharp resolution of the singular structures even with a relatively small number of particles. Moreover, in the two-species case, our method adeptly captures the blowing-up solution for the component with lower chemotactic sensitivity, a feature not observed in other works.

**Keywords:** Patlak-Keller-Segel chemotaxis systems, two-species chemotaxis, particle method, finite-difference schemes, blowup.

**AMS subject classification:** 65M75, 65M06, 76M28, 92C17, 35M10.

*Department of Mathematics, North Carolina State University, Raleigh, NC 27695, USA; chertock@math.ncsu.edu

†Shenzhen International Center for Mathematics, Southern University of Science and Technology (SUSTech), Shenzhen, 518055, PR China; cuism@sustech.edu.cn

‡Department of Mathematics, Shenzhen International Center for Mathematics, and Guangdong Provincial Key Laboratory of Computational Science and Material Design, Southern University of Science and Technology (SUSTech), Shenzhen 518055, PR China; alexander@sustech.edu.cn

§Shenzhen International Center for Mathematics, Southern University of Science and Technology (SUSTech), Shenzhen, 518055, PR China; wangcx2017@mail.sustech.edu.cn

# 1 Introduction

We consider the two-dimensional (2-D) two-species Patlak-Keller-Segel (PKS) type chemotaxis system:

$$\begin{cases} (\rho_1)_t + \chi_1 \nabla \cdot (\rho_1 \nabla c) = \nu_1 \Delta \rho_1, & \text{(1.1a)} \\ (\rho_2)_t + \chi_2 \nabla \cdot (\rho_2 \nabla c) = \nu_2 \Delta \rho_2, & \text{(1.1b)} \\ \tau c_t = \nu \Delta c + \gamma_1 \rho_1 + \gamma_2 \rho_2 - \zeta c, & \text{(1.1c)} \end{cases}$$

where $\boldsymbol{x} = (x, y)^\top \in \Omega \subset \mathbb{R}^2$ are the spatial variables, $t$ is time, $\rho_1$ and $\rho_2$ represent the cell densities of two non-competing species, $c$ is the concentration of the chemoattractant, $\chi_2 > \chi_1 > 0$ are the chemotactic sensitivity parameters, $\nu_1$, $\nu_2$, and $\nu$ are the diffusion coefficients, $\gamma_1$ and $\gamma_2$ represent chemoattractant production rates, and $\zeta$ represents chemoattractant decay rate ($\nu_1$, $\nu_2$, $\nu$, $\gamma_1$, $\gamma_2$, and $\zeta$ are positive constants). The parameter $\tau$ is either 0 or 1, corresponding to the case of parabolic-elliptic or parabolic-parabolic coupling, respectively. The system (1.1) is considered subject to certain initial data and the homogeneous Neumann boundary conditions.

The original single-species PKS chemotaxis model, which is obtained from the system (1.1) by setting $\rho_2 \equiv 0$, was first introduced in [32, 33, 37] and later extended to the two-species system (1.1) in [42]. Analytical investigations followed in [18, 24, 25, 29–31, 36, 41]. Depending on the initial data, boundary conditions, and parameter values, the solution may either converge to a constant steady state or develop singular structures (blow up in finite time). In blowup scenarios, different blowup time scales are anticipated for the two densities, with $\rho_2$ possibly blowing up faster than $\rho_1$. However, as proved in [24, 25], simultaneous blowup is the only possibility in the parabolic-elliptic case ($\tau = 0$), even though different scalings may exist for the two species. This poses a significant challenge in developing accurate and robust numerical methods for (1.1).

To the best of our knowledge, the first numerical method for (1.1) was introduced in [34], where the system (1.1) was solved a second-order hybrid finite-volume-finite-difference method proposed in [8] for the single-species PKS system. It was observed in [34] that when $\chi_2 \gg \chi_1$, the cell densities $\rho_1$ and $\rho_2$ exhibit different blowup behaviors: $\rho_2$ develops a $\delta$-type singularity, whereas $\rho_1$ undergoes algebraic blowup. This observation was numerically validated by conducting a very careful mesh refinement study. However, the obtained results were misleading since only algebraic growth—not blowup—of $\rho_1$ could be observed due to inadequate resolution (even on a very fine mesh). A fourth-order hybrid finite-volume-finite-difference method developed in [8] helped only slightly to enhance the resolution. More recently, in [13] an adaptive moving mesh (AMM) finite-volume semi-discrete upwind method was introduced to enhance the approximation of singular structures of $\rho_1$ in the two-species chemotaxis system. Despite this advancement, the numerical experiments reported in [13] show that even the AMM method failed to accurately capture the $\rho_1$-component of the blowing-up solution when $\chi_2 \gg \chi_1$.

In this paper, we offer a hybrid finite-difference-particle (FDP) approach for capturing the singular behavior of solutions of (1.1). In order to achieve a high resolution of both components of the blowing up solution ($\rho_1$ and $\rho_2$), we employ a sticky particle method introduced in [3, 14] in the context of pressureless gas dynamics equations, to the chemotaxis equations (1.1a) and (1.1b), while applying a second-order finite-difference (FD) semi-discrete scheme for solving the chemoattractant equation (1.1c).

Sticky particle methods belong to a class of deterministic particle methods, which provide a diffusion-free (or low diffusion) alternative to Eulerian methods for a variety of time-dependent

PDEs; see, e.g., [4,14] and references therein. In these methods, the numerical solution is sought as a linear combination of Dirac distributions ($\delta$-functions), whose positions and coefficients represent the locations and weights of the particles, respectively. The solution is then found by following the time evolution of the locations and weights of the particles according to a system of ODEs obtained by considering a weak formulation of the studied PDEs. Even though over the years deterministic particle methods were mainly used to numerically solve purely convective equations (see, e.g., [19, 39, 40] and references therein), the range of applicability of these methods was extended to treat convection-diffusion and other types of equations (see, e.g., [2,6,15,19–23,35,39]). Several approaches have been explored for treating diffusion terms in particle methods. One of the widely used treatments is the random walk approach [17,28], in which the diffusion operator is naturally approximated by adding a Wiener process to the motion of each particle. This way, the diffusion only affects the positions of particles—not their weights. A drawback of the random walk method, like other stochastic methods, is that its accuracy is very low, and reasonable resolutions can be achieved only if a very large number of realizations is used, which would make the particle method for the PKS-type systems extremely inefficient. Among the deterministic approaches, the one we have successfully implemented in this paper is a weighted particles method [21, 22, 35], which is both efficient and accurate. In this method, the diffusion is first approximated by an integral operator, which is then treated as a source term that affects the particle weights—not their positions.

As mesh-free, particle methods are quite flexible as the particle positions are self-adapted to the local flow. This, however, comes at the expense of the regularity of the particle distribution: inter-particle distances typically change in time, and just as particles may cluster, they may also spread away from each other. This may lead to a poor resolution of the computed solution and a low efficiency of the particle method. The latter is related to the fact that the time step for the ODE solver used to evolve the particle system in time depends generally on the distance between the neighboring particles. Thus, the success of deterministic particle methods relies upon an accurate and efficient particle redistribution algorithm, which ensures that different parts of the computed solution are adequately resolved. A large variety of re-meshing techniques has been proposed (see, e.g., [4, 7, 9, 11, 15, 16, 20, 23, 38] to name a few) including particle merger approach used in [11, 16, 20]. Particle merger becomes crucial in cases when the solution naturally develops sharp spikes or even $\delta$-type singularities. In these cases, the clustering particles must be merged into heavier particles located in the center of mass of the merged particles: this is the key feature of the sticky particle methods, which were successfully applied to the pressureless gas dynamics equations [14], dusty gas flows [5], and the PKS-type system in this paper.

The success of the proposed hybrid FDP method hinges on the accurate and efficient computations of the values of $c$ at the particle locations and the projection of the particle approximations onto the nodes of the FD grid. The former is achieved with the help of a global piecewise linear approximation of $c$ (this technique is borrowed from the finite-volume methods; also see the finite-volume-particles methods in [5, 14]), while for the latter one, we introduce a new particle-grid projection approach.

The paper is organized as follows. In §2, we give a brief overview of the weighted particle method for convection-diffusion equations. In §3, we introduce a hybrid FDP method, whose components—a novel sticky particle method for the cell densities equations and a second-order FD scheme for the chemoattractant equations—are described in §3.1 and §3.2, respectively. Details of the projection between the particle and grid data, which needs to be performed in the hybridization algorithm, are discussed in §3.3. In §4, we demonstrate the performance of the hybrid FDP

method on a number of challenging numerical examples designed to demonstrate the capability of the proposed method to resolve the blowup solution behavior with high resolution. Finally, we conclude the paper in §5 by summarizing our contributions.

# 2 Weighted Particle Method: an Overview

In this section, we briefly describe the weighted particle method for 2-D convection-diffusion equations. We consider the following model problem:

$$\rho_t + \nabla \cdot (\rho \boldsymbol{u}) = \nu \Delta \rho, \quad \boldsymbol{x} \in \Omega \subset \mathbb{R}^2, \quad t > 0, \tag{2.1}$$

subject to the initial data

$$\rho(\boldsymbol{x}, 0) = \rho_0(\boldsymbol{x}). \tag{2.2}$$

Here, $\rho(\boldsymbol{x}, t)$ is an unknown function, $\boldsymbol{u}(\boldsymbol{x}, t) = (u(\boldsymbol{x}, t), v(\boldsymbol{x}, t))^\top$ is the given velocity field, $\nu$ is a positive diffusion coefficient, and $\rho_0(\boldsymbol{x})$ is a given function. Notice that equations (1.1a) and (1.1b) would read as the convection-diffusion equation (2.1) if one replaces $\nabla c$ there with a given velocity field. Dependence of (1.1a) and (1.1b) on the chemoattractant equation (1.1c) makes the development of particle methods for (1.1a) and (1.1b) substantially more challenging, as discussed in §3.1, where we develop a new sticky particle method for chemotaxis equations.

We aim to find an approximate solution of (2.1)–(2.2) as a linear combination of Dirac $\delta$-functions,

$$\widehat{\rho}\,(\boldsymbol{x}, t) = \sum_{i=1}^{N} w_i(t)\, \delta(\boldsymbol{x} - \boldsymbol{x}_i(t)), \tag{2.3}$$

where $\boldsymbol{x}_i(t)$ represents the location of the $i$-th particle, $w_i(t)$ denotes its weight, and $N$ is the total number of particles. We would like to emphasize that this concept of particles represents a mathematical abstraction, differing from the physical concept of particles of specific materials.

We begin with the initialization of the particle approximation (2.3). To this end, we divide $\Omega$ into a set of non-overlapping subdomains $\{\Omega_i(0)\}_{i=1}^N$:

$$\Omega = \bigcup_{i=1}^{N} \Omega_i(0) \quad \text{and} \quad \Omega_i(0) \cap \Omega_j(0) = \emptyset \ \ \forall i \neq j.$$

We set the initial location of the $i$-th particle, $\boldsymbol{x}_i(0)$, to be the center of mass of $\Omega_i(0)$. The corresponding initial weight is then given by $\int_{\Omega_i(0)} \rho(\boldsymbol{x}, 0)\, \mathrm{d}\boldsymbol{x}$, which we approximate using the midpoint rule resulting in

$$w_i(0) = \rho(\boldsymbol{x}_i(0), 0)\, |\Omega_i(0)|. \tag{2.4}$$

Following the lines of [4] (also see [21, 22, 35]), we replace the Laplacian operator $\Delta\rho$ on the right-hand side of (2.1) with its integral approximation so that we obtain the equation

$$\rho_t(\boldsymbol{x}, t) + \nabla \cdot \big(\rho(\boldsymbol{x}, t)\boldsymbol{u}(\boldsymbol{x}, t)\big) = \frac{\nu}{\sigma^2} \iint\limits_{\mathbb{R}^2} \eta_\sigma(\boldsymbol{x} - \boldsymbol{y}) \big(\rho(\boldsymbol{y}, t) - \rho(\boldsymbol{x}, t)\big)\, \mathrm{d}\boldsymbol{y}, \tag{2.5}$$

where $\sigma$ is a small positive number and

$$\eta_\sigma(\boldsymbol{x}) := \frac{1}{\sigma^2} \eta\Big(\frac{\boldsymbol{x}}{\sigma}\Big), \quad \eta(\boldsymbol{x}) = \frac{4}{\pi} e^{-|\boldsymbol{x}|^2}, \tag{2.6}$$

and substitute (2.3) into a weak form of (2.5)–(2.6) to end up with the following system of ODEs for the particle locations $\boldsymbol{x}_i(t)$, weights $w_i(t)$, and subdomain sizes $|\Omega_i(t)|$:

$$\begin{cases} \dfrac{\mathrm{d}}{\mathrm{d}t}\,\boldsymbol{x}_i(t) = \boldsymbol{u}(\boldsymbol{x}_i(t),t) =: \boldsymbol{u}_i(t) = (u_i(t),v_i(t))^\top, \\ \dfrac{\mathrm{d}}{\mathrm{d}t}\,w_i(t) = \dfrac{\nu}{\sigma^2}\displaystyle\sum_{j=1}^{N}\eta_\sigma\big(\boldsymbol{x}_i(t)-\boldsymbol{x}_j(t)\big)\big[w_j(t)|\Omega_i(t)| - w_i(t)|\Omega_j(t)|\big] =: \beta_i(t), \\ \dfrac{\mathrm{d}}{\mathrm{d}t}\,|\Omega_i(t)| = \nabla\cdot\boldsymbol{u}(\boldsymbol{x}_i(t),t)\,|\Omega_i(t)|. \end{cases} \tag{2.7}$$

The initial conditions for this ODE system are specified in (2.4).

The ODE system (2.7) is to be numerically integrated by an appropriate ODE solver. The time step $\Delta t$ should depend on the distance between nearby particles as the stability condition imposes that no particle trajectories should intersect within the time interval $[t, t+\Delta t]$.

In order to quantify this requirement, let us consider $i$-th and $j$-th particles for some $i$ and $j$ and assume, for the sake of simplicity, that the system (2.7) is numerically solved by the first-order forward Euler method. In this case, the particle trajectories are straight lines and can be described by the following parametric form with parameters $\tau_i$ and $\tau_j$:

$$\begin{cases} x = x_i(t) + \tau_i u_i(t), \\ y = y_i(t) + \tau_i v_i(t), \end{cases} \quad \text{and} \quad \begin{cases} x = x_j(t) + \tau_j u_j(t), \\ y = y_j(t) + \tau_j v_j(t). \end{cases}$$

It is easy to verify that these two straight lines intersect at the point that corresponds to

$$\begin{aligned} \tau_i &= \frac{v_i(t)(x_j(t)-x_i(t)) - u_i(t)(y_j(t)-y_i(t))}{u_i(t)v_j(t) - u_j(t)v_i(t)}, \\ \tau_j &= \frac{v_j(t)(x_j(t)-x_i(t)) - u_j(t)(y_j(t)-y_i(t))}{u_i(t)v_j(t) - u_j(t)v_i(t)}, \end{aligned} \tag{2.8}$$

unless the denominator $u_i(t)v_j(t) - u_j(t)v_i(t)$ vanishes, in which case these two lines are parallel. Notice that the $i$-th particle will arrive in this intersection point at time $t+\tau_i$ provided $\tau_i > 0$, while the $j$-th particle will be there at time $t+\tau_j$ provided $\tau_j > 0$. This leads to the following time step constraint:

$$\Delta t \le \begin{cases} \displaystyle\min_{(i,j):\tau_i>0,\,\tau_j>0} \{\max(\tau_i,\tau_j)\} & \text{if } \exists\,(i,j):\tau_i>0,\,\tau_j>0, \\ \infty, & \text{otherwise.} \end{cases} \tag{2.9}$$

**Remark 2.1** *In practice, in order to prevent division by very small numbers, one has to use the formulae in (2.8) only when $|u_i(t)v_j(t) - u_j(t)v_i(t)| > \mu$, where $\mu$ is a small positive number.*

Additional time step constraints are obtained by requiring the weights $w_i$ to remain nonnegative for all $i$ (this is extremely important when $\rho$ must remain nonnegative as in the studied case of chemotaxis systems), the size of subdomains $\Omega_i$ not to decay too fast (for instance, one may restrict their decay within one-time step by a factor of 2), and no particle to propagate too far in one time step. In the case of forward Euler time discretization, these restrictions read as

$$\Delta t \le \begin{cases} \displaystyle\min_{i:\beta_i(t)<0}\left\{-\frac{w_i(t)}{\beta_i(t)}\right\} & \text{if } \max_i\left\{-\frac{w_i(t)}{\beta_i(t)}\right\} > 0, \\ \infty, & \text{otherwise,} \end{cases} \tag{2.10}$$

$$\Delta t \le \begin{cases} \min\limits_{i:\nabla\cdot\boldsymbol{u}(\boldsymbol{x}_i(t),t)<0} \left\{-\dfrac{1}{2\,\nabla\cdot\boldsymbol{u}(\boldsymbol{x}_i(t),t)}\right\} & \text{if } \max\limits_i \left\{-\dfrac{1}{2\,\nabla\cdot\boldsymbol{u}(\boldsymbol{x}_i(t),t)}\right\} > 0, \\ \infty, & \text{otherwise,} \end{cases} \tag{2.11}$$

and

$$\Delta t \le \frac{\sqrt{\min_i |\Omega_i(0)|}}{\max_i \left(\max\{|u_i|,|v_i|\}\right)}, \tag{2.12}$$

respectively.

**Remark 2.2** *The time restrictions (2.9)–(2.11) are still valid if a high-order strong stability preserving (SSP) Runge-Kutta or multistep explicit method [26, 27] is used instead of the forward Euler method for time integration, since the SSP methods can be expressed as convex combinations of forward Euler steps.*

# 3 Hybrid FDP Method for (1.1)

We now turn our attention to the PKS-type system (1.1) and introduce an FDP method for its numerical solution. Specifically, the chemotaxis equations (1.1a) and (1.1b) are discretized using a sticky particle method (§3.1), while the chemoattractant concentration equation (1.1c) is approximated using a FD scheme (§3.2). The coupling between the two ingredients of the FDP methods is carried out using the projection techniques (§3.3)

## 3.1 Sticky Particle Method for Equations (1.1a) and (1.1b)

Recall that the chemotaxis equations (1.1a) and (1.1b) take the form of the convection-diffusion equation (2.1) with $\rho$ being either $\rho_1$ or $\rho_2$, $\nu = \nu_1$ or $\nu = \nu_2$, and $\boldsymbol{u} = \chi_1\nabla c$ or $\boldsymbol{u} = \chi_2\nabla c$. The corresponding particle solutions for $\rho_1$ and $\rho_2$ are sought in the form

$$\widehat{\rho}_1(\boldsymbol{x},t) = \sum_{i=1}^{N_1} w_i^1(t)\,\delta(\boldsymbol{x}-\boldsymbol{x}_i^1(t)) \quad \text{and} \quad \widehat{\rho}_2(\boldsymbol{x},t) = \sum_{i=1}^{N_2} w_i^2(t)\,\delta(\boldsymbol{x}-\boldsymbol{x}_i^2(t)) \tag{3.1}$$

with $\boldsymbol{x}_i^1(t)$ and $\boldsymbol{x}_i^2(t)$ being each species particle locations, $w_i^1(t)$ and $w_i^2(t)$ their corresponding weights, and $N_1$ and $N_2$ the total number of each species particles. We denote by $\Omega_i^1(t)$ and $\Omega_i^2(t)$ the subdomains occupied by the corresponding particles.

In principle, one can apply the weighted particle method from §2 to (1.1a) and (1.1b), in which the particle locations, their weights, and sizes of the corresponding subdomains evolve in time according to (2.7). However, when the solutions of (1.1a) and (1.1b) start developing spiky structures, the particles start clustering in the regions of large chemoattractant gradient and hence, using a constant $\sigma$ in (2.7) leads to an inaccurate approximation of the diffusion operator. One therefore has to use variable values of $\sigma$, which depend on the distance between the particles. In particular, we use $\sigma_{ij}^k = \sqrt{\left(|\Omega_i^k| + |\Omega_j^k|\right)/2}$, $k = 1, 2$, so that the system (2.7) for $\rho_1$ and $\rho_2$ reads

as

$$\begin{cases} \dfrac{\mathrm{d}}{\mathrm{d}t}\boldsymbol{x}_i^k = (u_i^k, v_i^k)^\top, \quad k = 1, 2, \\ \dfrac{\mathrm{d}}{\mathrm{d}t} w_i^k = \nu \displaystyle\sum_{j=1}^{N_k} \frac{1}{(\sigma_{ij}^k)^2}\, \eta_{\sigma_{ij}^k}\big(\boldsymbol{x}_i^k - \boldsymbol{x}_j^k\big)\big[w_j^k|\Omega_i^k| - w_i^k|\Omega_j^k|\big], \quad k = 1, 2, \\ \dfrac{\mathrm{d}}{\mathrm{d}t}|\Omega_i^k| = r_i^k|\Omega_i^k|, \quad k = 1, 2. \end{cases} \tag{3.2}$$

Here, $(u_i^k, v_i^k)^\top \approx \chi_k \nabla c(x_i^k(t), y_i^k(t), t)$ and $r_i^k \approx \chi_k \Delta c(x_i^k(t), y_i^k(t), t)$, which will be obtained in §3.3.1 below. Notice that all of the indexed quantities in (3.2) depend on $t$, but we have omitted this dependence for the sake of brevity. Time dependence of indexed quantities will be also omitted below unless it is necessary to emphasize it in the discussion context.

It should be observed that choosing variable $\sigma_{ij}^k$ is not sufficient to make numerical integration of the ODE system (3.2) practically feasible as the time step restriction (2.9) would lead to $\Delta t \to 0$, when $\rho_1$ and $\rho_2$ approaching the point mass concentration.

In order to overcome this difficulty, we present a new sticky particle method for the chemotaxis equations (1.1a) and (1.1b). The basic idea of sticky particle methods is to coalesce clustering particles into a "heavier" particle located at their center of mass. In this paper, we intoduce a new particle merger strategy, which is implemented in two steps. Namely, at each time level $t$, we first identify pairs of particles whose trajectories are about to intersect by the next time level $t + \Delta t$ and merge them before the time evolution step. We then evolve the particles from $t$ to $t + \Delta t$ and coalesce those particles, which have clustered upon the completion of the evolution step (the second merger step was used in [5, 11, 14, 16, 20]).

In order to implement the merger, we introduce an auxiliary "merger" Cartesian grid consisting of small cells of the size about $\frac{1}{4}\min_i |\Omega_i(0)|$ and assume that at a certain time level $t$ no "merger" cell contain more than one particle. We then compute the time step $\Delta t$ based on the two-species version of the time step restrictions (2.10)–(2.12), but not (2.9), which, as we have mentioned, may be impractically too restrictive. Equipped with this $\Delta t$, we proceed with the following steps.

**Merger Step 1.** We identify those pairs of the same species particles, whose trajectories are about to intersect before time $t + \Delta t$. Let us assume that $\{(\boldsymbol{x}_i^k, w_i^k, |\Omega_i^k|), (\boldsymbol{x}_j^k, w_j^k, |\Omega_j^k|)\}$ is one of such pairs ($k = 1$ or 2), that is, $\tau_i^k > 0$, $\tau_j^k > 0$, and $\max\{\tau_i^k, \tau_j^k\} < \Delta t$, where $\tau_i^k$ and $\tau_j^k$ are given by the two-species version of (2.8). We then add the weights of these two particles, combine their subdomains, and replace the two particles with one heavier particle located at the center of mass of the replaced particles:

$$\big\{(\boldsymbol{x}_i^k, w_i^k, |\Omega_i^k|), (\boldsymbol{x}_j^k, w_j^k, |\Omega_j^k|)\big\} \quad \longrightarrow \quad (\widetilde{\boldsymbol{x}}^k, \widetilde{w}^k, |\widetilde{\Omega}^k|)$$

with

$$\widetilde{\boldsymbol{x}}^k = \frac{w_i^k \boldsymbol{x}_i^k + w_j^k \boldsymbol{x}_j^k}{w_i^k + w_j^k}, \quad \widetilde{w}^k = w_i^k + w_j^k, \quad |\widetilde{\Omega}^k| = |\Omega_i^k| + |\Omega_j^k|.$$

Once the $i$-th and $j$-th particles of species $k$ have been merged, the total number of particles for this species reduces by one, the remaining particles are re-numbered, and Merger Step 1 is repeated for each species to ensure that no particle trajectories intersect within the current time step.

**Remark 3.1** *Notice that the process of searching for pairs of particles with potentially intersecting trajectories is computationally expensive if performed in a straightforward manner—looping through all particle pairs of species $k$ is $\mathcal{O}(N_k^2)$ expensive. However, the search mechanism can be made efficient by introducing another auxiliary Cartesian grid with cells of size $\min_i|\Omega_i(0)|$ and using the fact that the time step restriction (2.12) ensures that particles cannot propagate too far within one time step. One can then check the particles located in nearby auxiliary cells. This alternative implementation is only $\mathcal{O}(N_k)$ expensive for $k=1,2$.*

**Time Evolution.** The particle solution is evolved from time $t$ to $t+\Delta t$ by numerically solving (3.2). Recall that the system (1.1) is solved subject to the homogeneous Neumann boundary conditions, which imply that no particles should leave the computational domain $\Omega$. This is, however, not automatically guaranteed and we therefore develop a "pull-back" strategy of relocating the outside particles back on the domain boundary $\partial\Omega$ as follows: we move the outside particle to the closest point on $\partial\Omega$. Once all of the evolved particles are located in $\Omega$, one has to coalesce the clustering particles according to Merger Step 2.

If a Runge-Kutta ODE solver is employed (as in all of the numerical experiments presented in §4), then both "pull-back" and merger algorithms should be implemented at the end of each Runge-Kutta stage.

**Merger Step 2.** We find all of the auxiliary "merger" cells containing more than one particle from the same species and then merge them according to the following procedure. Let $C_{\rm mer}$ be one of such cells with two or more particles of species $k$ ($k=1$ or 2). Then, the particles of species $k$ located in $C_{\rm mer}$ are merged into a new particle, $(\widetilde{\boldsymbol{x}}^k,\widetilde{w}^k,|\widetilde{\Omega}^k|)$, located at the center of mass of the replaced particles and their weights and subdomain sizes are summed up:

$$\widetilde{\boldsymbol{x}}^k=\frac{\sum\limits_{i:\boldsymbol{x}_i^k\in C_{\rm mer}} w_i^k\boldsymbol{x}_i^k}{\sum\limits_{i:\boldsymbol{x}_i^k\in C_{\rm mer}} w_i^k},\qquad \widetilde{w}^k=\sum_{i:\boldsymbol{x}_i^k\in C_{\rm mer}} w_i^k,\qquad |\widetilde{\Omega}^k|=\sum_{i:\boldsymbol{x}_i\in C_{\rm mer}}|\Omega_i^k|.$$

**Remark 3.2** *We would like to point out that, by construction, the sticky particle method preserves the positivity of $\rho_1$ and $\rho_2$, which is a crucial property for the stability of numerical methods for PKS-type systems, as it was show in [10].*

## 3.2 Finite-Difference Scheme for Equation (1.1c)

In this section, we describe the second ingredient of our hybrid method—the FD scheme, which is used to numerically solve the chemoattractant concentration equation (1.1c). We restrict our consideration to the case of a rectangular computational domain $\Omega$. For general domains, one can still use FD schemes, but treatment of boundary conditions and grid points near the boundary becomes quite delicate (this is outside the scope of current paper).

We first split $\Omega$ into uniform rectangular cells $C_{\ell,m}$ of dimensions $\Delta x$ and $\Delta y$ and denote the cell centers by $\boldsymbol{x}_{\ell,m}=(x_{\ell,m},y_{\ell,m})$. A second-order FD discretization of (1.1c) (or, a semi-discretization in the parabolic case with $\tau=1$) reads as

$$\tau\frac{\mathrm{d}}{\mathrm{d}t}c_{\ell,m}=\nu\left[\frac{c_{\ell+1,m}-2c_{\ell,m}+c_{\ell-1,m}}{(\Delta x)^2}+\frac{c_{\ell,m+1}-2c_{\ell,m}+c_{\ell,m-1}}{(\Delta y)^2}\right]+\gamma_1(\rho_1)_{\ell,m}+\gamma_2(\rho_2)_{\ell,m}-\zeta c_{\ell,m},\quad(3.3)$$

where $c_{\ell,m} :\approx c(\boldsymbol{x}_{\ell,m}, t)$.

If $\tau = 1$, then one need to numerically integrate the extended ODE system (3.2)–(3.3). Otherwise, if $\tau = 0$, (3.3) is a linear algebraic system with respect to $\{c_{\ell,m}\}$, which needs to be solved upon completion of each Runge-Kutta stage.

## 3.3 Projection Between the Particle and Grid Data

It should be obsevred that one has to project the data from/to the particle locations $\boldsymbol{x}_i^k$ to/from the grid nodes $\boldsymbol{x}_{\ell,m}$, when a meshless particle method is combined with a grid-based FD scheme. We introduce these mapping procedures in §3.3.1 and §3.3.2.

### 3.3.1 Computation of $\nabla c$ and $\Delta c$ at Particle Locations

In order to evolve particles in time according to (3.2), one has to compute velocities $(u_i^k, v_i^k)^\top$ and their divergences $r_i^k$ at the particle locations. Since these quantities are obtained using $\nabla c$ and $\Delta c$ and since the values $c_{\ell,m}$ are computed at the grid points, a projection of the grid data on the particle location has to be carried out. This can be done as follows.

First, we compute the point values of $c_x$, $c_y$, and $\Delta c$ at the grid points using the second-order FDs:

$$(c_x)_{\ell,m} = \frac{c_{\ell+1,m} - c_{\ell-1,m}}{2\Delta x}, \quad (c_y)_{\ell,m} = \frac{c_{\ell,m+1} - c_{\ell,m-1}}{2\Delta y},$$
$$(\Delta c)_{\ell,m} = \frac{c_{\ell+1,m} - 2c_{\ell,m} + c_{\ell-1,m}}{(\Delta x)^2} + \frac{c_{\ell,m+1} - 2c_{\ell,m} + c_{\ell,m-1}}{(\Delta y)^2},$$

then construct global (in space) piecewise linear interpolants for $c_x$, $c_y$, and $\Delta c$, which is in every cell $C_{\ell,m}$ defined by

$$\widetilde{c_x}(x,y) = (c_x)_{\ell,m} + \frac{(c_x)_{\ell+1,m} - (c_x)_{\ell-1,m}}{2\Delta x}(x - x_{\ell,m}) + \frac{(c_x)_{\ell,m+1} - (c_x)_{\ell,m-1}}{2\Delta y}(y - y_{\ell,m}),$$
$$\widetilde{c_y}(x,y) = (c_y)_{\ell,m} + \frac{(c_y)_{\ell+1,m} - (c_y)_{\ell-1,m}}{2\Delta x}(x - x_{\ell,m}) + \frac{(c_y)_{\ell,m+1} - (c_y)_{\ell,m-1}}{2\Delta y}(y - y_{\ell,m}),$$
$$\widetilde{\Delta c}(x,y) = (\Delta c)_{\ell,m} + \frac{(\Delta c)_{\ell+1,m} - (\Delta c)_{\ell-1,m}}{2\Delta x}(x - x_{\ell,m}) + \frac{(\Delta c)_{\ell,m+1} - (\Delta c)_{\ell,m-1}}{2\Delta y}(y - y_{\ell,m}),$$

and finally, for each particle location $\boldsymbol{x}_i^k$, $k = 1, 2$, we obtain

$$u_i^k = \chi_k \widetilde{c_x}(x_i^k, y_i^k), \quad v_i^k = \chi_k \widetilde{c_y}(x_i^k, y_i^k), \quad r_i^k = \chi_k \widetilde{\Delta c}(x_i^k, y_i^k). \tag{3.4}$$

### 3.3.2 Computation of $\rho_1$ and $\rho_2$ at Grid Points

In order to evolve $c$ in time according to (3.3), one has to recover the density grid values $(\rho_1)_{\ell,m}$ and $(\rho_2)_{\ell,m}$ from the particle distributions (3.1). This can be conducted in the following three steps.

**Step 1.** We compute the point values $\rho_1$ and $\rho_2$ at the particle locations $\boldsymbol{x}_i^k$ by dividing the particle weight $w_i^k$ by the corresponding subdomain sizes $|\Omega_i^k|$, that is, we set $\rho_i^k = w_i^k / |\Omega_i^k|$.

**Step 2.** For each particle satisfying $\boldsymbol{x}_i^k \in C_{\ell,m}$, we compute the distance from this particle to the cell center $\boldsymbol{x}_{\ell,m}$:

$$(d_i^k)_{\ell,m} := |\boldsymbol{x}_i^k - \boldsymbol{x}_{\ell,m}|, \tag{3.5}$$

and evaluate the grid values of $\rho_1$ and $\rho_2$ at the cell center $\boldsymbol{x}_{\ell,m}$ using a distance-based weighted averaging:

$$(\rho_k)^*_{\ell,m}=\frac{\sum\limits_{\boldsymbol{x}_i^k\in C_{\ell,m}}\rho_i^k/(d_i^k)_{\ell,m}}{\sum\limits_{\boldsymbol{x}_i^k\in C_{\ell,m}}1/(d_i^k)_{\ell,m}},\qquad k=1,2. \tag{3.6}$$

If there is no particles of species $k$ in cell $C_{\ell,m}$, we set $(\rho_k)^*_{\ell,m}=0$.

**Step 3.** In the cells containing no particles, the value $(\rho_k)^*_{\ell,m}=0$ may be very inaccurate. The therefore replace the values computed in **Step 2** with:

$$(\rho_k)_{\ell,m}=\begin{cases}(\rho_k)^*_{\ell,m} & \text{if } \exists\, i:\boldsymbol{x}_i^k\in C_{\ell,m},\\ \dfrac{(\rho_k)^*_{\ell+1,m}+(\rho_k)^*_{\ell-1,m}+(\rho_k)^*_{\ell,m+1}+(\rho_k)^*_{\ell,m-1}}{4+2\sqrt{2}} & \\ \quad+\dfrac{(\rho_k)^*_{\ell+1,m+1}+(\rho_k)^*_{\ell+1,m-1}+(\rho_k)^*_{\ell-1,m+1}+(\rho_k)^*_{\ell-1,m-1}}{4+4\sqrt{2}}, & \text{otherwise.}\end{cases}$$

where the latter expression is the distance-based weighted averaging over neighboring cells.

**Remark 3.3** *It should be observed that there are other ways to recover grid values of the computed solution from its particle distribution when the solution is smooth; see, e.g., [4]. However, after the spiky structure is developed, most of these methods are based on a certain regularization of the $\delta$-functions and hence lead to a substantial decrease of the maximum values of $\rho_1$ and $\rho_2$. The method we have used in Step 1 seems to be the only robust option.*

**Remark 3.4** *Note that some of the values $d_i^k$ defined in (3.5) may be very small or even zero. We therefore need to desingularize the computation in (3.6) to prevent division by small numbers. This is done by replacing (3.5) with*

$$d_i^k=\max\left\{d_{\min},|\boldsymbol{x}_i^k-\boldsymbol{x}_{\ell,m}|\right\},$$

*where $d_{\min}$ is a small positive number taken to be $\min(\Delta x,\Delta y)/16$ in all of the numerical examples reported in §4.*

# 4 Numerical Examples

In this section, we demonstrate the performance of the proposed hybrid FDP method and its capability of capturing the blowing up solutions of the PKS-type system (1.1) with high resolution.

Recall that the proposed method employs three different meshes for distinct purposes: a mesh used in the FD scheme ($C_{\ell,m}$), a mesh used as initial particle subdomains $\Omega_i(0)$, and a mesh used for Merger Step 2 ($C_{\text{mer}}$). In the following numerical examples, we use uniform meshes with $\Delta:=\Delta x=\Delta y$ and keep the ratio between these three mesh sizes fixed. Specifically, by "numerical results obtained on a mesh of size $\Delta$", we imply the combination of a mesh of size $\Delta$ for the FD scheme, a mesh of size $\Delta/4$ for initial particle subdomains, and a mesh of size $\Delta/8$ for the merger.

For time evolution, we use the three-stage third-order SSP Runge-Kutta method [26,27]. The time step is selected using the stability restrictions introduced in (2.10)–(2.12). We remind the reader that once the final time solution has been computed, the point values of $c$ are available,

while the point values of $\rho_1$ and $\rho_2$ need to be recovered as described in **Steps 1 and 2** in §3.3.2. In order to visualize the obtained solution and conduct the experimental convergence study, one may use, for instance, the MATLAB built-in function `scatteredInterpolant`.

## 4.1 Parabolic-Parabolic Case ($\tau = 1$)

**Example 1—Accuracy Test**

The primary objective of this example is to experimentally check the accuracy of the proposed hybrid FDP method.

We consider the system (1.1) with $\tau = 1$, $\nu = 10$, $\chi_1 = 5$, $\chi_2 = 60$, $\gamma_1 = \gamma_2 = \zeta = \nu_1 = \nu_2 = 1$, and subject to the following initial conditions:

$$\rho_1(x, y, 0) = \rho_2(x, y, 0) = 500\,\mathrm{e}^{-100(x^2+y^2)}, \quad c(x, y, 0) \equiv 1, \quad (x, y) \in \Omega = [-1, 1] \times [-1, 1].$$

We compute the numerical solutions until time $t = 2 \times 10^{-4}$ using various resolutions with $\Delta = 2/15$, $2/20$, $2/25$, $2/30$, $2/40$, $2/50$, $2/60$, $2/80$, $2/100$, and $2/120$. Given the numerical solutions obtained on meshes of sizes $\Delta$, $\Delta/2$, and $\Delta/4$, we compute the $L^1$- and $L^2$-errors and estimate the corresponding experimental convergence rates using the following Runge formulae:

$$L^p\text{-error} \approx \frac{\|(\cdot)^{\frac{\Delta}{2}} - (\cdot)^{\frac{\Delta}{4}}\|_{L^p}^2}{\left|\|(\cdot)^{\Delta} - (\cdot)^{\frac{\Delta}{2}}\|_{L^p} - \|(\cdot)^{\frac{\Delta}{2}} - (\cdot)^{\frac{\Delta}{4}}\|_{L^p}\right|}, \quad \text{rate} \approx \log_2\left(\frac{\|(\cdot)^{\Delta} - (\cdot)^{\frac{\Delta}{2}}\|_{L^p}}{\|(\cdot)^{\frac{\Delta}{2}} - (\cdot)^{\frac{\Delta}{4}}\|_{L^p}}\right), \quad p = 1, 2,$$

where $(\cdot)^{\Delta}$ denotes the numerical results obtained on a mesh of size $\Delta$.

The computed $L^1$- and $L^2$-errors and the corresponding experimental convergence rates for $\rho_1$, $\rho_2$, and $c$ are presented in Table 4.1, where one can see that the second order of accuracy is achieved.

| | $\rho_1$ | | | | $\rho_2$ | | | | $c$ | | | |
|---|---|---|---|---|---|---|---|---|---|---|---|---|
| $\Delta$ | $L^1$-error | rate | $L^2$-error | rate | $L^1$-error | rate | $L^2$-error | rate | $L^1$-error | rate | $L^2$-error | rate |
| 2/60 | 2.94e-2 | 1.95 | 1.35e-1 | 1.88 | 7.70e-2 | 2.20 | 2.94e-1 | 2.43 | 1.80e-4 | 1.78 | 4.12e-4 | 2.00 |
| 2/80 | 1.55e-2 | 2.00 | 7.75e-2 | 1.85 | 4.52e-2 | 1.64 | 1.96e-1 | 1.70 | 1.06e-4 | 1.81 | 3.43e-4 | 1.65 |
| 2/100 | 1.04e-2 | 1.93 | 4.48e-2 | 1.93 | 2.19e-2 | 2.43 | 8.40e-2 | 2.68 | 7.33e-5 | 1.75 | 1.65e-4 | 1.93 |
| 2/120 | 6.20e-3 | 2.07 | 2.55e-2 | 2.10 | 1.93e-2 | 2.11 | 6.63e-2 | 2.06 | 4.52e-5 | 1.87 | 1.06e-4 | 1.99 |

Table 4.1: Example 1: The $L^1$- and $L^2$-errors and the corresponding convergence rates.

**Example 2—Two-Species Blowup at the Center of the Domain**

In this example, we consider the same initial-boundary value problem (IBVP) as in Example 1, but compute its numerical solution until much larger times $t = 5 \times 10^{-4}$ and $10^{-3}$. The densities $\rho_1$ and $\rho_2$ obtained on a mesh of size $\Delta = 1/20$ are plotted in Figure 4.1. The results are comparable to the ones in [13, Example 3] and [34]: Both $\rho_1$ and $\rho_2$ exhibit blowup behavior, and the solution of $\rho_2$ blows up faster.

This example is challenging in the sense that excessive numerical viscosity may smear the singularity, leading to a failure to capture the blowup behavior. Due to the low-dissipation nature

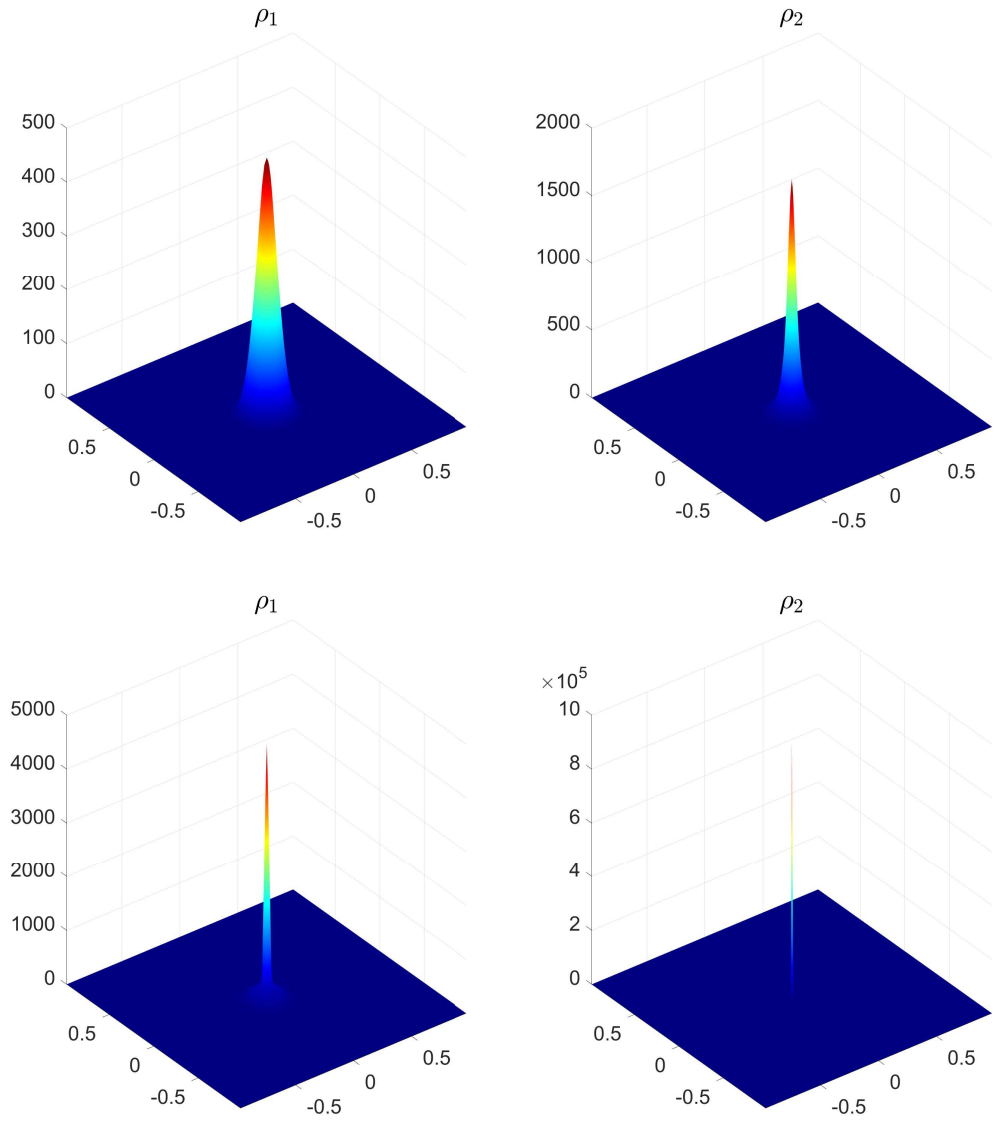


Figure 4.1: Example 2: $\rho_1(\boldsymbol{x}, 0.0005)$ (upper left), $\rho_2(\boldsymbol{x}, 0.0005)$ (upper right), $\rho_1(\boldsymbol{x}, 0.001)$ (lower left), and $\rho_2(\boldsymbol{x}, 0.001)$ (lower right), obtained using the hybrid FDP method with $\Delta = 1/20$.

of the sticky particle method, the hybrid FDP method provides a higher resolution: The maximum values of $\rho_1$ and $\rho_2$ are respectively $4.7355 \times 10^3$ and $9.6558 \times 10^5$, as compared to $3.5758 \times 10^3$ and $2.8726 \times 10^5$ reported in [13, Example 3].

### Example 3—Single-Species Blowup at the Corner of the Domain

The third example taken from [10] is designed to demonstrate the ability of the proposed hybrid FDP method to capture the blowup behavior away from the center of the initial Gaussian-shaped cell density.

We consider the single-species PKS system

$$\begin{cases} \rho_t + \nabla \cdot (\rho \nabla c) = \Delta \rho, \\ c_t = \Delta c + \rho - c, \end{cases} \tag{4.1}$$

subject to following initial conditions:

$$\rho(x,y,0) = 500\,\mathrm{e}^{-100[(x-0.25)^2+(y-0.25)^2]},\quad c(x,y,0)\equiv 0,\quad (x,y)\in\Omega=[-0.5,0.5]\times[-0.5,0.5]. \tag{4.2}$$

It has been proved in [30] that when the total mass of $\rho$ is below a certain threshold, the density $\rho$ can only blow up at the boundary of the computational domain. This is indeed the case for the IBVP (4.1)–(4.2).

We employ the hybrid FDP method to compute the solution on a mesh of size $\Delta = 1/20$. The density $\rho$ at different times is shown in Figure 4.2, and the particle locations $\{(x_i(t), y_i(t))\}$ at times $t = 0.02$ and 0.1 are depicted in Figure 4.3. As one can observe, the behavior of the computed solution matches the theoretical results established in [30]: The mass of $\rho$ first moves to the boundary and then concentrates at the corner where the solution blows up.

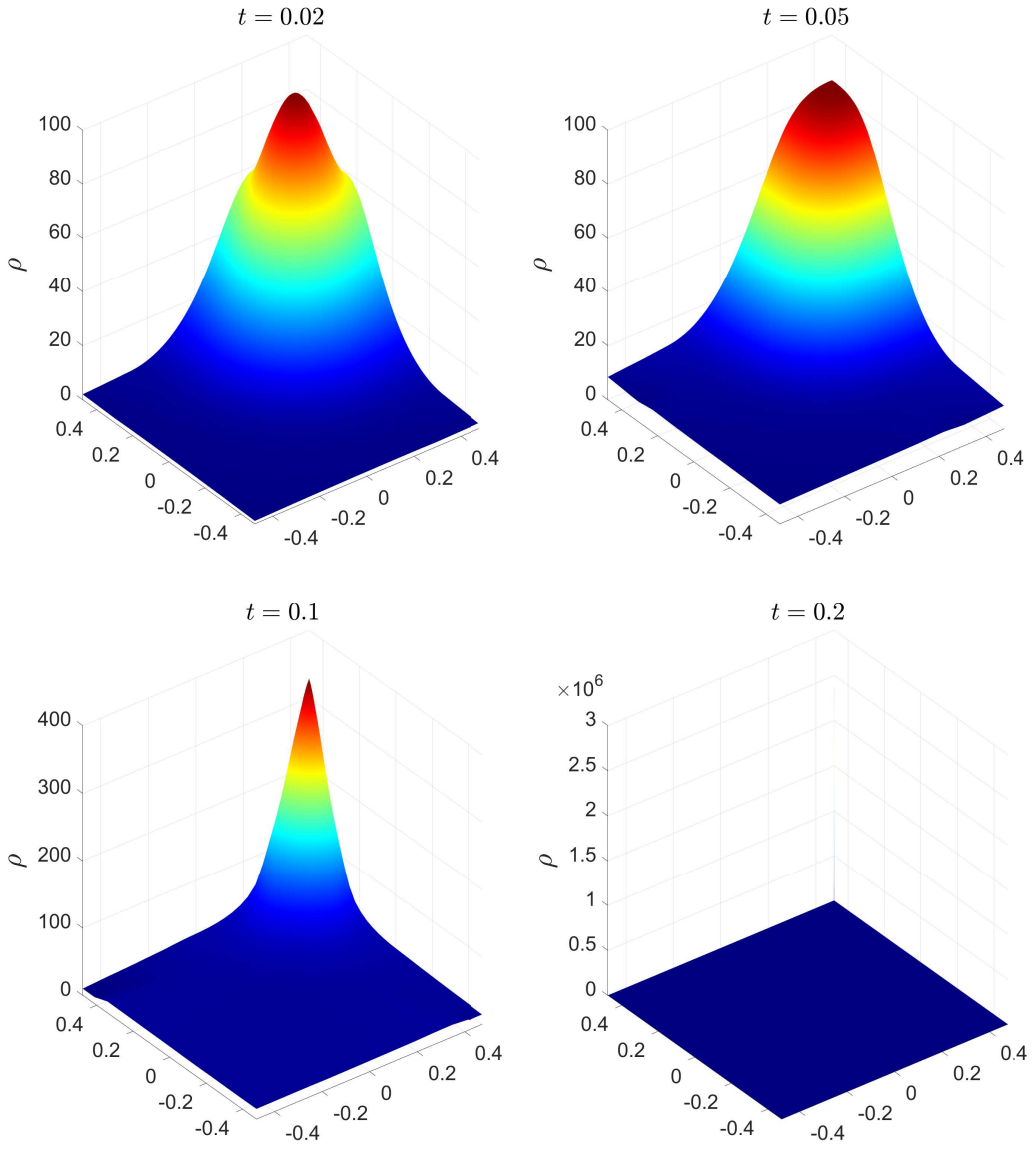


Figure 4.2: Example 3: $\rho(\boldsymbol{x}, 0.02)$ (upper left), $\rho(\boldsymbol{x}, 0.05)$ (upper right), $\rho(\boldsymbol{x}, 0.1)$ (lower left), and $\rho(\boldsymbol{x}, 0.2)$ (lower right), obtained using the hybrid FDP method with $\Delta = 1/20$.

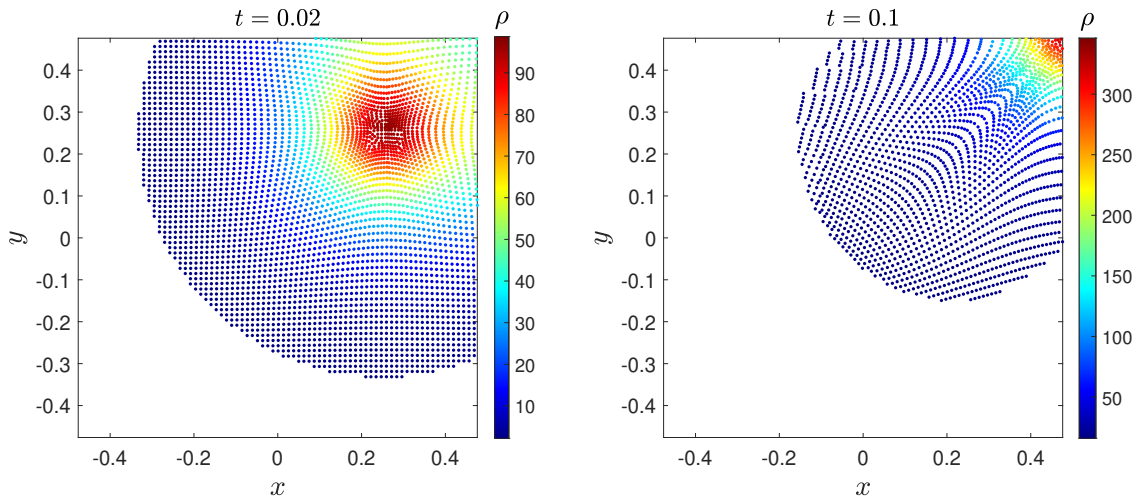


Figure 4.3: Example 3: particle locations at $t = 0.02$ (left) and $t = 0.1$ (right), obtained using the hybrid FDP method with $\Delta = 1/20$. The color indicates the value of $w_i(t)/|\Omega_i(t)|$.

**Example 4—Single-Species Blowup in the Interior of the Domain**

We consider the same IBVP as in Example 3, but with different initial conditions:

$$\rho(x,y,0) = 1000\,\mathrm{e}^{-100[(x-0.25)^2+(y-0.25)^2]}, \quad c(x,y,0) \equiv 0, \quad (x,y) \in \Omega = [-0.5,0.5] \times [-0.5,0.5].$$

In this case, the total mass of $\rho$ is greater than the threshold, and the solution is expected to blow up in the interior of the computational domain.

We compute the solution by the proposed hybrid FDP method on a mesh of size $\Delta = 1/20$ until the final time $t = 0.1$. In Figure 4.4, we plot the density $\rho$ at different times together with the location of the "dominating" particle at $t = 0.1$ (by that time the solution has blown up and most of the mass is concentrated at the "dominating" particle), which is, as one can clearly see, inside the domain. This result is consistent with both the theoretical result in [30] and the numerical results reported in [1, 12].

## 4.2 Parabolic-Elliptic Case ($\tau = 0$)

In this section, we consider an extremely challenging numerical example introduced in [34].

**Example 5—Two-Species Blowup at the Center of the Domain**

In this example, we consider the system (1.1) with $\tau = 0$, $\gamma_1 = \gamma_2 = \zeta = \nu_1 = \nu_2 = \nu = \chi_1 = 1$, $\chi_2 = 20$, and subject to the following initial conditions:

$$\rho_1(x,y,0) = \rho_2(x,y,0) = 50\,\mathrm{e}^{-100(x^2+y^2)}, \quad (x,y) \in \Omega = [-1,1] \times [-1,1].$$

According to [24, 25], both $\rho_1$ and $\rho_2$ are expected to blow up *simultaneously* in finite time. However, as demonstrated in [8,13,34], $\rho_1$ and $\rho_2$ are expected to undergo different blowup patterns: While $\rho_2$ develops a $\delta$-type singularity, $\rho_1$ grows up algebraically.

We compute the solution until the same (as in [8, 13, 34]) final time $t = 0.0033$ using the proposed hybrid FDP method on a mesh of size 1/20. The densities $\rho_1$ and $\rho_2$, obtained at times

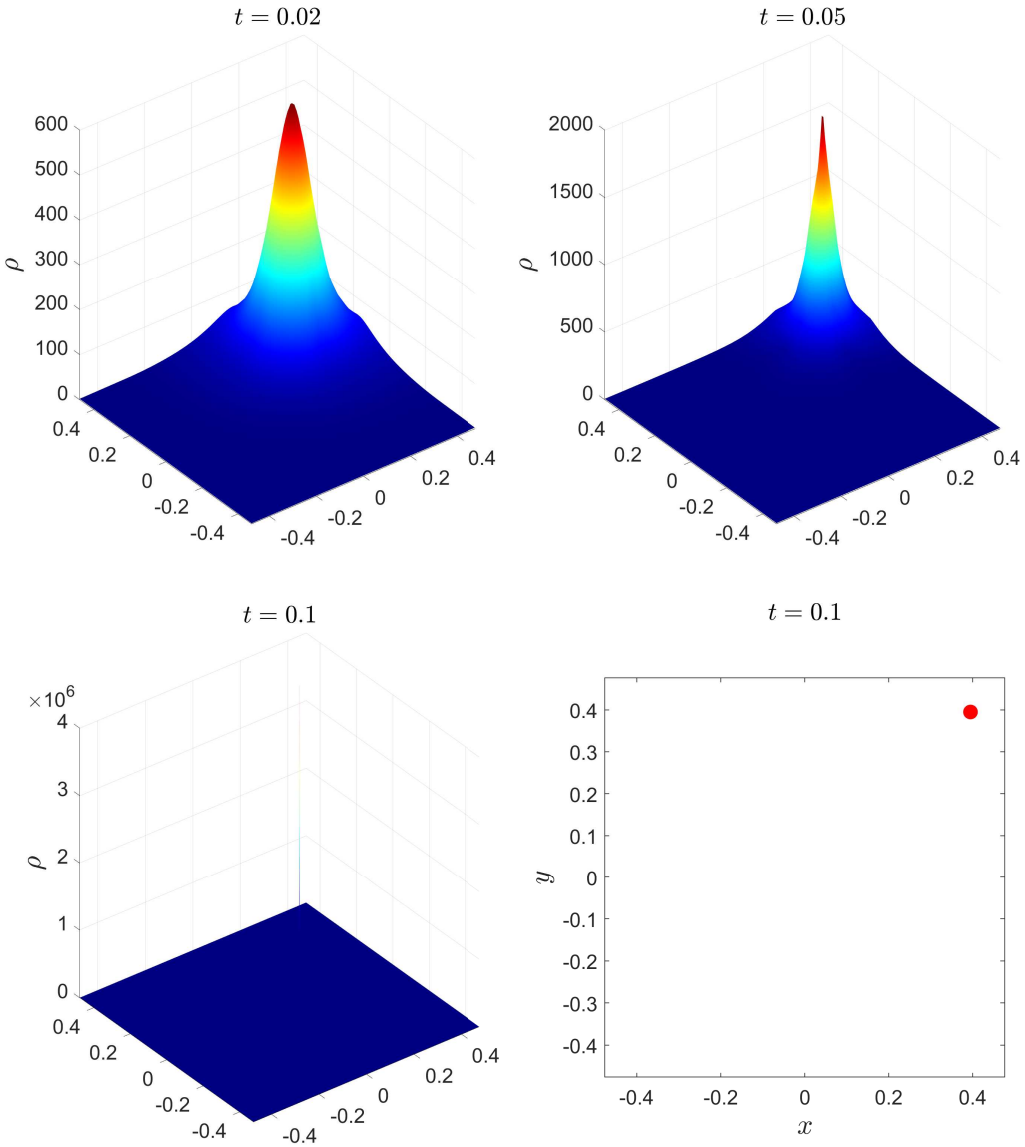


Figure 4.4: Example 4: $\rho(\boldsymbol{x}, 0.02)$ (upper left), $\rho(\boldsymbol{x}, 0.05)$ (upper right), $\rho(\boldsymbol{x}, 0.1)$ (lower left), and the location of the "dominating" particle at $t = 0.1$ (lower right), obtained using the hybrid FDP method with $\Delta = 1/20$.

$t = 0.003$ and $0.0033$ are shown in Figure 4.5. We would like to emphasize that achieving a high resolution of blowup behavior in $\rho_1$ is a particularly challenging task. Neither the second-order hybrid finite-volume-finite-difference [34] nor its fourth-order version [8] were able to clearly capture the algebraic blowup of $\rho_1$. Some improvement was achieved in [13], where an AMM finite-volume upwind method was developed and applied to the studied IBVP, but the maximum of the blowed up $\rho_1$ on the finest mesh there was about 75 (compare with the corresponding maximum of $\rho_2$, which was about $1.3 \times 10^5$). One can observe in Figure 4.5, our hybrid FDP method leads to a considerably higher resolution of $\rho_1$ compared to the schemes in [8, 13, 34]: The maximum values of $\rho_1$ and $\rho_2$ at $t = 0.0033$ are about $6.2 \times 10^4$ and $1.6 \times 10^5$, respectively. The qualitative jump in the resolution of $\rho_1$ is attributed to the low-dissipation nature of the sticky particle method.

In Figure 4.6, we present time evolution of the maximum values of $\rho_1$ and $\rho_2$ for $\Delta = 1/15$,

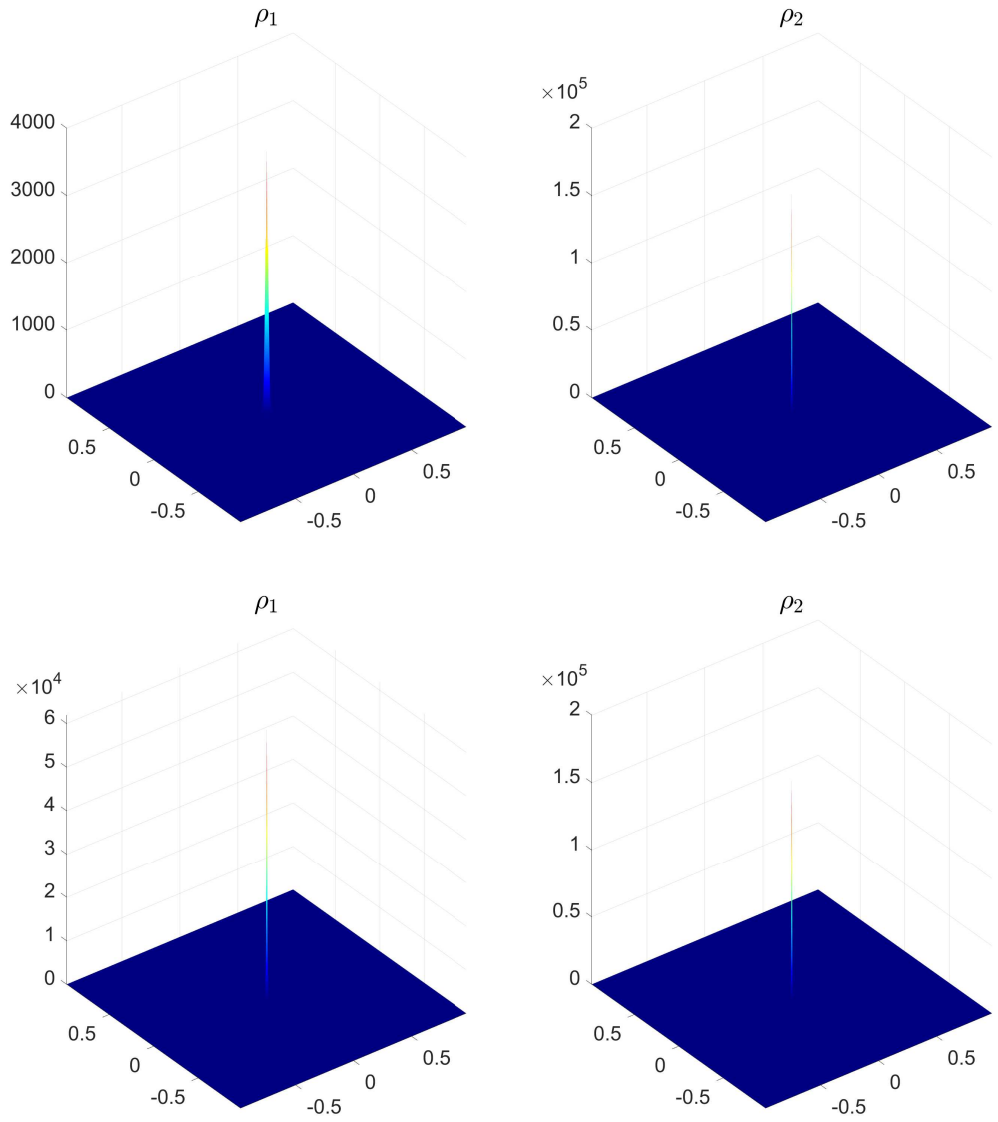


Figure 4.5: Example 5: $\rho_1(\boldsymbol{x}, 0.003)$ (upper left), $\rho_2(\boldsymbol{x}, 0.003)$ (upper right), $\rho_1(\boldsymbol{x}, 0.0033)$ (lower left), and $\rho_2(\boldsymbol{x}, 0.0033)$ (lower right), obtained using the hybrid FDP method with $\Delta = 1/20$.

1/20, 1/25, and 1/30. As one can see, by refining the mesh from $\Delta = 1/15$ to 1/30, the maximum of $\rho_1$ increases by a factor of about 6, which exhibits a much faster increase compared those obtained in [8, 13, 34]. This clearly demonstrates that the hybrid FDP method outperforms its grid-based counterparts.

It should also be observed that the blowup time for the PKS-type system (1.1) cannot be obtained theoretically and therefore it is important to determine it numerically. Figure 4.6 suggests that the solution computed by the hybrid FDP method blows up by time $t = 0.00294$, at which the entire mass of the second species concentrates at one point (noticably, this time is the same for different $\Delta$). We showcase this by zooming the maximum curves in Figure 4.6 at the time interval $[0.028, 0.003]$, which helps one to better observe a difference between the blowup behavior of the first and second species. We note that the observed blowup time ($t = 0.00294$) is smaller the one ($t = 0.0033$) reported in [13]; see also [8,34]. This is attributed to a low-dissipation nature

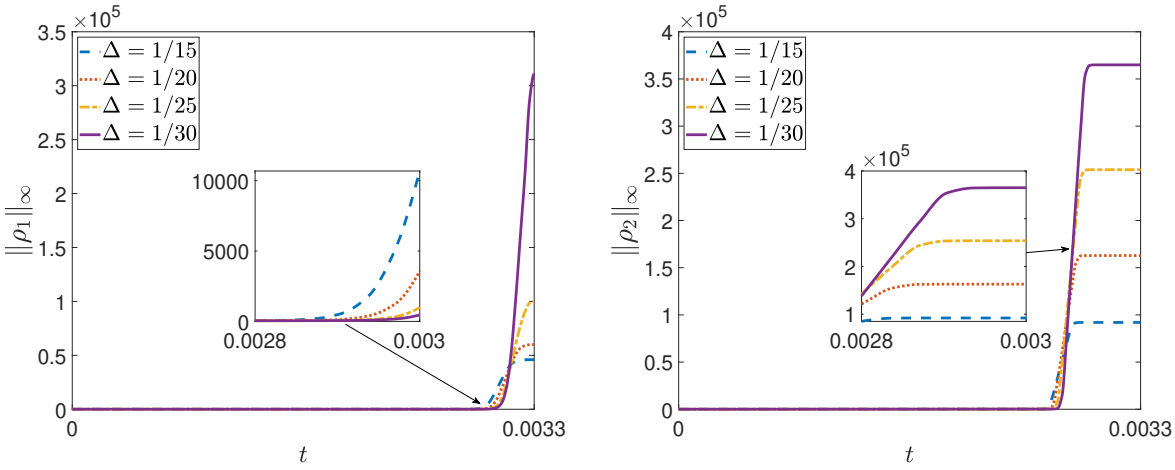


Figure 4.6: Example 5: The maximums of $\rho_1$ (left) and $\rho_2$ (right) computed using $\Delta = 1/15$, $1/20$, $1/25$, and $1/30$.

of the sticky particle method as the grid-based methods in [8,13,34] contain numerical dissipation, which causes a delay in blowup for both $\rho_1$ and $\rho_2$.

# 5 Conclusion

In this paper, we have designed a novel hybrid finite-difference-particle (FDP) methods for the Patlak-Keller-Segel-type chemotaxis systems in either parabolic-parabolic or parabolic-elliptic form. Our approach uses a sticky particle method for the cell density equation(s) and a second-order finite-difference scheme for the chemoattractant equation. The performance of the proposed hybrid FDP methods have been examined on a comprehensive series of challenging examples. Thanks to the low-dissipation nature of the sticky particle method, the proposed scheme is particularly adept at capturing the blowing up solutions in both one- and two-species cases. The numerical results obtained using the hybrid FDP methods exhibit superior resolution compared to traditional grid-based methods.

# Acknowledgments

The work of A. Chertock was supported in part by NSF grant DMS-2208438. The work of S. Cui was supported in part by Shenzhen Science and Technology Program (grant No. RCJC20221008092757098). The work of A. Kurganov was supported in part by NSFC grant 12171226 and by the fund of the Guangdong Provincial Key Laboratory of Computational Science and Material Design (No. 2019B030301001).

# References

[1] D. ACOSTA-SOBA, F. GUILLÉN-GONZÁLEZ, AND J. R. RODRÍGUEZ-GALVÁN, *An unconditionally energy stable and positive upwind DG scheme for the Keller-Segel model*, J. Sci.

Comput., 97 (2023), pp. Paper No. 18, 27.

[2] M. Bergdorf, G.-H. Cottet, and P. Koumoutsakos, *Multilevel adaptive particle methods for convection-diffusion equations*, Multiscale Model. Simul., 4 (2005), pp. 328–357.

[3] F. Bouchut and F. James, *Duality solutions for pressureless gases, monotone scalar conservation laws, and uniqueness*, Comm. Partial Differential Equations, 24 (1999), pp. 2173–2189.

[4] A. Chertock, *A practical guide to deterministic particle methods*, in Handbook of numerical methods for hyperbolic problems, vol. 18 of Handb. Numer. Anal., Elsevier/North-Holland, Amsterdam, 2017, pp. 177–202.

[5] A. Chertock, S. Cui, and A. Kurganov, *Hybrid finite-volume-particle method for dusty gas flows*, SMAI J. Comput. Math., 3 (2017), pp. 139–180.

[6] A. Chertock, C. R. Doering, E. Kashdan, and A. Kurganov, *A fast explicit operator splitting method for passive scalar advection*, J. Sci. Comput., 45 (2010), pp. 200–214.

[7] A. Chertock, P. Du Toit, and J. E. Marsden, *Integration of the EPDiff equation by particle methods*, ESAIM Math. Model. Numer. Anal., 46 (2012), pp. 515–534.

[8] A. Chertock, Y. Epshteyn, H. Hu, and A. Kurganov, *High-order positivity-preserving hybrid finite-volume-finite-difference methods for chemotaxis systems*, Adv. Comput. Math., 44 (2018), pp. 327–350.

[9] A. Chertock and A. Kurganov, *On a practical implementation of particle methods*, Appl. Numer. Math., 56 (2006), pp. 1418–1431.

[10] ——, *A second-order positivity preserving central-upwind scheme for chemotaxis and haptotaxis models*, Numer. Math., 111 (2008), pp. 169–205.

[11] A. Chertock, A. Kurganov, and Y. Liu, *Finite-volume-particle methods for the two-component Camassa-Holm system*, Commun. Comput. Phys., 27 (2020), pp. 480–502.

[12] A. Chertock, A. Kurganov, M. Lukáčová-Medviďová, and c. N. Özcan, *An asymptotic preserving scheme for kinetic chemotaxis models in two space dimensions*, Kinet. Relat. Models, 12 (2019), pp. 195–216.

[13] A. Chertock, A. Kurganov, M. Ricchiuto, and T. Wu, *Adaptive moving mesh upwind scheme for the two-species chemotaxis model*, Comput. Math. Appl., 77 (2019), pp. 3172–3185.

[14] A. Chertock, A. Kurganov, and Y. Rykov, *A new sticky particle method for pressureless gas dynamics*, SIAM J. Numer. Anal., 45 (2007), pp. 2408–2441.

[15] A. Chertock and D. Levy, *Particle methods for dispersive equations*, J. Comput. Phys., 171 (2001), pp. 708–730.

[16] A. Chertock, J.-G. Liu, and T. Pendleton, *Elastic collisions among peakon solutions for the Camassa-Holm equation*, Appl. Numer. Math., 93 (2015), pp. 30–46.

[17] A. J. CHORIN, *Numerical study of slightly viscous flow*, J. Fluid Mech., 57 (1973), pp. 785–796.

[18] C. CONCA, E. ESPEJO, AND K. VILCHES, *Remarks on the blowup and global existence for a two species chemotactic Keller-Segel system in* $\mathbb{R}^2$, European J. Appl. Math., 22 (2011), pp. 553–580.

[19] G.-H. COTTET AND P. D. KOUMOUTSAKOS, *Vortex methods. Theory and practice*, Cambridge University Press, Cambridge, 2000.

[20] S. CUI, A. KURGANOV, AND A. MEDOVIKOV, *Particle methods for PDEs arising in financial modeling*, Appl. Numer. Math., 93 (2015), pp. 123–139.

[21] P. DEGOND AND S. MAS-GALLIC, *The weighted particle method for convection-diffusion equations. I. The case of an isotropic viscosity*, Math. Comp., 53 (1989), pp. 485–507.

[22] P. DEGOND AND F.-J. MUSTIELES, *A deterministic approximation of diffusion equations using particles*, SIAM J. Sci. Statist. Comput., 11 (1990), pp. 293–310.

[23] J. D. ELDREDGE, A. LEONARD, AND T. COLONIUS, *A general deterministic treatment of derivatives in particle methods*, Journal of Computational Physics, 180 (2002), pp. 686–709.

[24] E. ESPEJO, K. VILCHES, AND C. CONCA, *Sharp condition for blow-up and global existence in a two species chemotactic Keller-Segel system in* $\mathbb{R}^2$, European J. Appl. Math., 24 (2013), pp. 297–313.

[25] E. E. ESPEJO, A. STEVENS, AND T. SUZUKI, *Simultaneous blowup and mass separation during collapse in an interacting system of chemotactic species*, Differential Integral Equations, 25 (2012), pp. 251–288.

[26] S. GOTTLIEB, D. KETCHESON, AND C.-W. SHU, *Strong stability preserving Runge-Kutta and multistep time discretizations*, World Scientific Publishing Co. Pte. Ltd., Hackensack, NJ, 2011.

[27] S. GOTTLIEB, C.-W. SHU, AND E. TADMOR, *Strong stability-preserving high-order time discretization methods*, SIAM Rev., 43 (2001), pp. 89–112.

[28] M. GRIEBEL AND M. A. SCHWEITZER, *A particle-partition of unity method for the solution of elliptic, parabolic, and hyperbolic PDEs*, SIAM J. Sci. Comput., 22 (2000), pp. 853–890 (electronic).

[29] M. A. HERRERO AND J. J. L. VELÁZQUEZ, *Chemotactic collapse for the Keller-Segel model*, J. Math. Biol., 35 (1996), pp. 177–194.

[30] ———, *A blow-up mechanism for a chemotaxis model*, Ann. Scuola Norm. Sup. Pisa Cl. Sci. (4), 24 (1997), pp. 633–683.

[31] T. HILLEN AND K. J. PAINTER, *A user's guide to PDE models for chemotaxis*, J. Math. Biol., 58 (2009), pp. 183–217.

[32] E. F. KELLER AND L. A. SEGEL, *Initiation of slime mold aggregation viewed as an instability*, J. Theoret. Biol., 26 (1970), pp. 399–415.

[33] ——, *Model for chemotaxis*, J. Theor. Biol., 30 (1971), pp. 225–234.

[34] A. KURGANOV AND M. LUKÁČOVÁ-MEDVIĎOVÁ, *Numerical study of two-species chemotaxis models*, Discrete Contin. Dyn. Syst. Ser. B, 19 (2014), pp. 131–152.

[35] S. MAS-GALLIC AND F. POUPAUD, *Approximation of the transport equation by a weighted particle method*, Transport Theory and Stat. Phys., 17 (1988), pp. 311–345.

[36] H. G. OTHMER AND A. STEVENS, *Aggregation, blowup, and collapse: the ABCs of taxis in reinforced random walks*, SIAM J. Appl. Math., 57 (1997), pp. 1044–1081.

[37] C. S. PATLAK, *Random walk with persistence and external bias*, Bull. Math. Biophys., 15 (1953), pp. 311–338.

[38] C. S. PESKIN, *The immersed boundary method*, Acta Numer., 11 (2002), pp. 479–517.

[39] E. G. PUCKETT, *Vortex methods: an introduction and survey of selected research topics*, in Incompressible computational fluid dynamics: trends and advances, Cambridge Univ. Press, Cambridge, 2008, pp. 335–407.

[40] P.-A. RAVIART, *An analysis of particle methods*, in Numerical methods in fluid dynamics (Como, 1983), vol. 1127 of Lecture Notes in Math., Springer, Berlin, 1985, pp. 243–324.

[41] T. SENBA AND T. SUZUKI, *Parabolic system of chemotaxis: blowup in a finite and the infinite time*, Methods Appl. Anal., 8 (2001), pp. 349–367. IMS Workshop on Reaction-Diffusion Systems (Shatin, 1999).

[42] G. WOLANSKY, *Multi-components chemotactic system in the absence of conflicts*, European J. Appl. Math., 13 (2002), pp. 641–661.